

4D study of liquid binder penetration dynamics in pharmaceutical powders using synchrotron X-ray micro computed tomography

Sima Zeinali Danalou ^a, Xiao Fan Ding ^b, Ning Zhu ^{a,b,c}, Heather N. Emady ^d, Lifeng Zhang ^{a,*}

^a Department of Chemical and Biological Engineering, University of Saskatchewan, SK, Canada

^b Department of Biomedical Engineering, University of Saskatchewan, SK, Canada

^c Canadian Light Source Inc., SK, Canada

^d School for Engineering of Matter, Transport and Energy, Arizona State University, AZ, USA



ARTICLE INFO

Keywords:

Pharmaceutical powders
Wet granulation
Penetration
Droplet imbibition
Droplet spreading
synchrotron X-ray imaging

ABSTRACT

The properties of pharmaceutical powders, and the liquid binder, directly influence the penetration behavior in the wet granulation process of the pharmaceutical industry. Conventional methods encounter challenges in understanding this fast process. In this work, an emerging synchrotron-based X-ray imaging technique (having fast imaging capability) was employed to investigate the internal process from 2D and 3D to real-time (*in-situ* with *ms* time intervals) 3D (also considered 4D) perspectives. Two commonly used excipients (lactose monohydrate (LMH) and microcrystalline cellulose (MCC)) were used to make binary mixtures with acetaminophen (APAP) as the active pharmaceutical ingredient (API). Isopropanol and water were employed as liquid binders in the single droplet impact method. Results showed that for most of the mixtures, the porosity increased at higher fractions of APAP. MCC mixtures experienced less agglomeration and more uniform pore distribution than LMH ones, resulting in a faster droplet penetration with isopropanol. Moreover, the imbibition-spreading studies showed that isopropanol penetration in MCC powders followed more unidirectional vertical movement than horizontal spreading. Our results also demonstrated that simultaneous granulation of LMH with water resulted in much slower penetration. This study revealed that synchrotron X-ray imaging can investigate 3D internal pore structures and how they affect the quantitatively real-time internal penetration dynamics.

1. Introduction

Wet granulation is one of the essential unit operations in the pharmaceutical industry, by which particles agglomerate with the addition of a liquid binder. Wetting and nucleation, consolidation and growth, and attrition and breakage are the three key steps in the wet granulation process (Iveson et al., 2001). Feed powder and binder properties directly affect granulation (Hapgood et al., 2002). Thus, understanding the interaction between liquid binder droplets and powder mixtures is vital for further improvements in pharmaceutical granulation.

It is well recognized that the powder mixing quality directly impacts the final products in many industries, including pharmaceuticals, cement, food, and plastics. Particle segregation is desirable in the case of separating specific components; however, it could lead to various problems. As an example, in the pharmaceutical industry, if the ratio of the active component is not the same in all tablets, the desired quality of the tablets would not be met, resulting in significant economic losses

(Asachi et al., 2018). The physical properties, including particle size and morphology, significantly impact powder segregation (Oka et al., 2017). Among them, the leading cause of powder segregation is particle size differences (Aulton, 2002). Generally, segregation is lower in cohesive powders (Furukawa et al., 2016). Particles larger than 250 µm are typically free-flowing, but as the size decreases below 100 µm, powders become cohesive, and flow issues are likely (Aulton, 2002). Particle size affects cohesive interactive forces between particles related to electrostatic, van der Waals, and hydrophilic interactions (Furukawa et al., 2016). As a result of decreased particle size and increasing cohesion, agglomeration occurs, which is a common phenomenon during the first stages of mixing (Venables and Wells, 2001).

Powder packing is another important factor affecting pharmaceutical processing and product properties. There are correlations between pore structure, bed porosity, permeability, and fluid flow or liquid mass transfer within the porous media (Dias et al., 2004). Porosity is primarily determined by particle size, size distribution, and particle shape under specified packing circumstances. In the literature, many numerical

* Corresponding author.

E-mail address: Lifeng.zhang@usask.ca (L. Zhang).

Nomenclature			
AR	aspect ratio	ρ_{bed}	particle bulk density, (g/cm ³)
CDA	constant drawing area	σ	standard deviation
D_0	initial droplet width, (mm)	σ_0^2	variance of desired material at complete segregation
\bar{D}	dimensionless width	σ^2	variance of desired material at actual mixing condition
d_s	surface mean diameter, (μm)	σ_r^2	variance of desired material at complete mixing
d_{50}	median particle size, (μm)		
\bar{H}	dimensionless height		
MI	mixing index		
R_{imb}	imbibition rate, (s^{-1})		
RSD	relative standard deviation		
r_d	droplet radius, (mm)		
\bar{t}	dimensionless time		
V_0	initial droplet volume, (μL^3)		
$V(t)$	droplet volume remaining at the bed surface, (μL^3)		
ρ_p	particle skeletal density, (g/cm ³)		
Abbreviation			
APAP	acetaminophen		
API	active pharmaceutical ingredient		
BMIT	Biomedical Imaging and Therapy Facility		
CLS	Canadian Light Source		
FOV	field of view		
LMH	lactose monohydrate		
LMHF	lactose monohydrate fine		
MCC	microcrystalline cellulose		
MCCF	microcrystalline cellulose fine		

studies have been conducted to predict powder mixtures' porosity (Clarke et al., 2002; Forny et al., 2011; Fu et al., 2019). Due to the fact that industrial powders often deviate from ideal assumptions of spherical, smooth, and solid particles, the models would not provide a reliable estimate. For example, rod-shaped, tiny, and cohesive particles would pose additional challenges to predicting their bulk behavior, such as porosity (He et al., 2013). Therefore, it is imperative to develop a method to directly observe the internal structure of powders to advance knowledge on the porosity of powder mixtures with irregular particle properties.

While the droplet penetrates the powder bed, a general combination of spreading and imbibition occurs in the wetting stage of wet granulation (Mundozah et al., 2018). The porosity, size, orientation of the pores, and surface chemistry within the bed all contribute to the imbibition of a single drop into a porous substrate (Hapgood et al., 2002). Different methods have been employed to study the droplet penetration phenomenon into porous media, such as optical microscopes, high-speed imaging cameras, and scanning electron microscopy (SEM). Single droplet granule formation is a promising method that has been used in many studies on droplet penetration, granule formation, and formed granules (Charles-Williams et al., 2011; Emady et al., 2013, 2011; Gao et al., 2020, 2018). Gao et al. (2020, 2018) used a high-speed camera (Photron Fastcam-X 1024 PCI) to investigate granule formation mechanisms from pharmaceutical powders. Pan et al. (2021) recorded water droplet imbibition into a nanoporous carbon scaffold with an environmental scanning electron microscope (ESEM) at a rate of approximately 1/3 or 3 frames per second. Hapgood et al. (2002) used a Zeiss Stemi 2000 microscope with a Sony CCD camera and a JVC SVHS video recorder operating at 25 frames/s to film a single droplet penetrating into the powder. However, all mentioned techniques were not able to visualize the internal structure during the *in-situ* droplet penetration process. Studying the internal structures has received increasing attention recently, and this development was made possible by using the emerging capability of a synchrotron X-ray (e.g., higher photon flux and better light source of 3rd and 4th generation synchrotron technique, high speed detector system available, and the progress of high speed imaging processing system) to scan ultra-fast phenomena using time-resolved techniques (Marone et al., 2020). As an example, Gonçalves et al. (2022) recently used synchrotron X-ray imaging to observe water dynamics in porous and non-porous substrates and could provide a valuable framework for understanding wetting and evaporation in porous fabric substrates.

Pharmaceutical powders and droplet penetration within them, on the other hand, have rarely been investigated internally due to their

opaque nature and rapid processes (Li et al., 2019). Synchrotron X-ray imaging overcomes the problems and limitations of the conventional methods, such as light scattering, low spatial resolution, slow imaging, and sample damage (Gonçalves et al., 2022). Synchrotron X-ray imaging techniques (with a speed of approximately 2000 frames/s) allow for visualization of the powder and binder penetration inside the powder media through high-resolution 2D- and 3D- images.

The objective of this study was to employ synchrotron X-ray imaging techniques to characterize the mixing quality and 3D internal properties of the static powder bed of a model two-component system consisting of acetaminophen with microcrystalline cellulose or lactose monohydrate, mainly focusing on particle size effects. And, more specifically, this work studied how powder bed microstructures affect the internal real-time 3D (*in-situ* 3D imaging, or 4D) single droplet penetration dynamics by two binders of water and isopropanol.

2. Materials and methods

2.1. Materials

Acetaminophen (APAP) as an active pharmaceutical ingredient and two commonly used excipients, microcrystalline cellulose (MCC) and lactose monohydrate (LMH), as fillers were used to prepare binary mixtures. APAP, MCC, and LMH were ordered from Hebei Jiheng Pharmaceutical, FMC BioPolymers, and Foremost Farms, respectively.

2.2. Characterization

The median particle size and surface mean diameter were measured by a particle size analyzer (Malvern Mastersizer 2000 S, Malvern Instruments, UK). The particle skeletal density was determined with a gas multi-pycnometer (QuantaChrome, Boynton Beach, FL, USA). A 100 mL graduated cylinder was used to measure the particle bulk density. Bulk density was calculated as the mass per unit volume, after loading the cylinder with powder through a plastic funnel at a height of 2 cm from the top of the cylinder, leveling the top surface, and then measuring the weight of the powder. The same condition was repeated for three replicates for each powder sample. Aspect ratio (maximum width/minimum width), representing the particle morphology, was measured based on thresholding the particles in ImageJ (National Institutes of Health, USA). The microstructures of the powders were examined by SEM (Hitachi Field Emission Scanning Electron Microscope – FESEM Model SU8010, Hitachi, Japan), where the powders were precoated with a gold layer. Contact angle represents the wettability of the powder with the

liquid. The contact angles are taken from our previous work and measured based on the Washburn capillary rise (WCR) method (Li et al., 2021).

2.3. Sample preparation

Firstly, to avoid large agglomerates, pure powders were sieved through a sieve with an opening size of 1 mm (US mesh # 16). To investigate the effects of powder properties on binary mixtures and droplet penetration patterns, binary mixtures were prepared with two different excipients with two particle sizes (fine and coarse). Fine lactose monohydrate (LMHF) and fine microcrystalline cellulose (MCCF) were obtained by sieving the coarse LMH and MCC powders through a sieve with a 38 µm opening size (US mesh # 400). Bulk binary mixtures were prepared with the mass fractions detailed in Table 1. Binary mixtures of about 16 g were loaded into a 10 mL vial and placed on a mixer (Fisherbrand™ Digital Vortex Mixer 80863022, Fisher Scientific) and mixed at 2000 rpm for 10 min. This mixing condition was fixed for all powders, and it was tested for the sample with a composition of 50LF-50A as a base model. In order to characterize mixing quality, Lacey's mixing index (Lacey, 1954), based on the variance between the active component concentration at perfect mixing and total segregation, was employed in this work, and this mixing index (MI) is given by Equation (1):

$$MI = \frac{\sigma_0^2 - \sigma^2}{\sigma_0^2 - \sigma_r^2} \quad (1)$$

$$\sigma^2 = \frac{1}{n-1} \sum_{i=1}^n (x_i - \bar{x})^2 \quad (2)$$

where σ_0^2 , σ^2 and σ_r^2 are the concentration variance of APAP at complete segregation, the actual mixing condition, and a random mixture in the almost completely mixed state ($\sigma_r^2 \approx 0$), respectively; n is the total sample number; x_i is the composition of APAP in the 50LF-50A mixture; and \bar{x} is the mean average mass concentration of APAP. If MI is close to 1, it means the binary system experienced uniform mixing. For this purpose, 10 mg was sampled from each of the ten layers of the vial, as shown in Fig. 1. UV-vis spectrometry was used to determine the APAP content. In the experiments, 10 mg powder was dissolved in 10 mL of deionized water (as solvent), and then 45 µL of the solution was diluted to 5 mL with deionized water. The diluted solution was assayed at 232 nm. Two trials were performed, and based on the absorbance and corresponding APAP concentrations along the vial, the MI was measured as roughly 98 % for 50LF-50A for each trial.

For synchrotron X-ray imaging, the powder mixture from the bulk container (16 g) was poured through a plastic funnel into a vial with a height of 2 cm and an inner diameter of 1 cm. To have a consistent pouring velocity, the funnel was positioned at a fixed height of 1 cm

Table 1
Mass percentage of pharmaceutical powders in binary mixtures.

Sample No.	Sample Name	Excipient Mass Percent (%)	APAP Mass Percent (%)
1	90L-10A	LMH	90 10
2	80L-20A	LMH	80 20
3	50L-50A	LMH	50 50
4	90LF-10A	LMHF	90 10
5	80LF-20A	LMHF	80 20
6	50LF-50A	LMHF	50 50
7	90M-10A	MCC	90 10
8	80M-20A	MCC	80 20
9	50M-50A	MCC	50 50
10	90MF-10A	MCCF	90 10
11	80MF-20A	MCCF	80 20
12	50MF-50A	MCCF	50 50

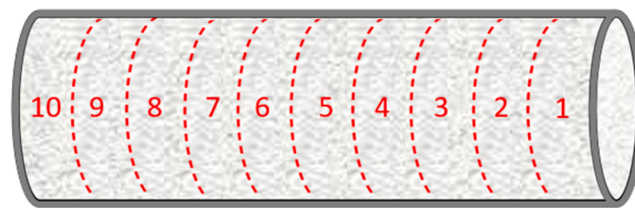


Fig. 1. The schematic diagram of the binary powder mixture container.

from the top of the vial. Prior to imaging, the powder surface was leveled to gain a smooth surface.

2.4. Penetration dynamics measurements

While the droplet imbibes into the powder, its volume decreases. The volume remaining at the surface ($V(t)$) can be calculated by the following equation (Gonçalves et al., 2022):

$$V(t) = \frac{\pi r_d^3}{12} \left(\frac{2 - 3\cos\theta + \cos^3\theta}{\sin^3\theta} \right) \quad (3)$$

where r_d and θ are the droplet radius and the dynamic contact angle, respectively. Due to the simultaneous wetting and nucleation, at the end of penetration, $V(t)$ would not reach zero.

When a droplet comes into contact with a porous substrate, imbibition occurs by a liquid moving into the substrate. Darcy's dimensional imbibition rate was measured to describe the imbibition rate as follows (Mundoza et al., 2018):

$$R_{imb} = \frac{\left(\frac{V_0 - V(t)}{V_0} \right)}{\left(\frac{D}{D_0} \right)^2} \quad (4)$$

where D_0 and V_0 are the initial droplet width and volume, respectively, and $V(t)$ and D are the droplet volume and width over time, respectively.

2.5. Synchrotron X-ray CT setup

Synchrotron X-ray CT experiments were performed at the Biomedical Imaging and Therapy (BMIT) Facility 05B1-1 bending magnet beamline at the Canadian Light Source (CLS), which is a third-generation synchrotron (Li et al., 2019). The X-ray projections were captured by indirect detection using a Hamamatsu AA-40 beam monitor (Hamamatsu, Japan) downstream from a 200 µm LuAG scintillator to convert X-rays transmitted from the sample to visible light, followed by a PCO.DIMAX HS4 camera (PCO AG, Germany). A filtered white beam provided high photon flux. The single droplet impact method was employed to study the penetration through different powder compositions. The liquid droplet was generated using a micropipette, and its volume was kept constant at 10 µL, and the needle's height was kept constant at 2.5 cm from the bed surface. The number of projections per CT for scanning the static powder and capturing the penetration process were 3000 and 500 projections, respectively. The exposure time of each projection was 1 ms. The field of view (FOV) was 11 mm × 4 mm (v × h) (see Fig. 2), and the effective pixel size was 5.5 µm. The schematic setup is shown in Fig. 3.

2.6. Post-processing and data analysis

UFO-KIT (Karlsruhe Institute of Technology (KIT), Germany) was used to perform tomographic reconstruction with phase retrieval (Faragó et al., 2022; Vogelgesang et al., 2016). Two sets of images, dark and flat, were collected to spatially normalize the images without the sample. Beam and flat images were captured with a beam present, and

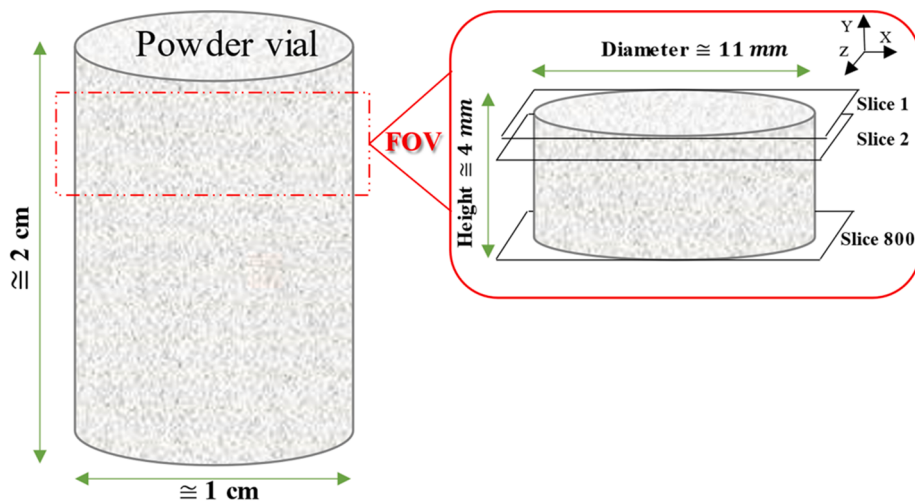


Fig. 2. Location and dimensions of the FOV.

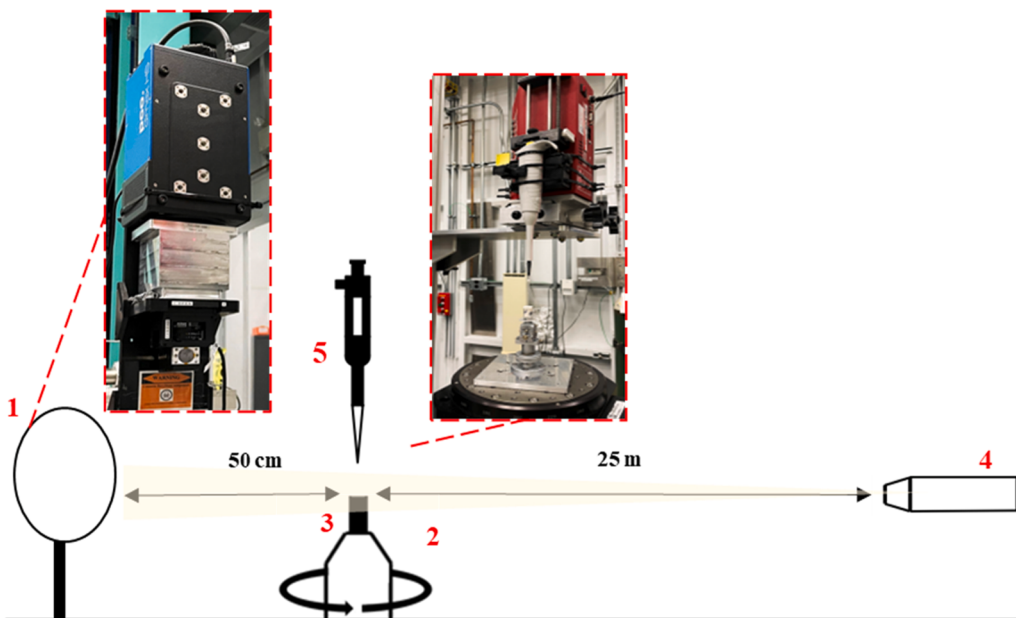


Fig. 3. Single drop experimental setup: 1) X-ray detector, 2) Rotary stage, 3) Sample vessel, 4) synchrotron X-ray beam, 5) Micropipettor and syringe pump.

dark images were captured without the beam. ImageJ (National Institutes of Health, USA) was used for thresholding, and Dragonfly version 2021.1 was used for 3D rendering and particle properties measurements (Objects Research Systems (ORS) Inc., Canada).

Particles with higher density absorb X-ray photons more and can be visually detected as areas with lighter grey color in the reconstructed image (Kalender, 2011). Hence, different gray value intensity ranges would be a common method for image segmentation. Fig. 4 shows a cross-sectional view, in which lower gray values correspond to the area with a lower density. Consequently, air (voidage), with the lowest density compared to the solid particles, will be present in a black-dark grey color. Otsu threshold, a widely used method in image processing, in Dragonfly, was employed to segment the air voids and particles. In this approach, the histogram's mean square errors were reduced in order to choose a single threshold value. More details about this common method can be found in other publications (Jianzhuang et al., 1991; Otsu, 1979). Considering the 3D volume image, the porosity was calculated by dividing the pore volume over the total volume of FOV.

3. Results and discussion

3.1. Physical properties of pharmaceutical powders

Table 2 presents the powder characterization, including median particle size (d_{50}), surface mean diameter (d_s), particle skeletal density (ρ_p), particle bulk density (ρ_{bed}), aspect ratio (AR), and contact angle with the liquid binders (isopropanol and deionized water). MCC had the largest size (110.4 μm), and LMHF had the smallest size (16.9 μm). APAP had a higher particle density compared to the excipients. Both MCC and MCCF had a higher wettability with isopropanol, and LMH had a higher wettability with water compared to LMHF. SEM images in Fig. 5 show that APAP and MCC particles were rod-shaped with higher AR, while LMH particles showed a different morphology with lower AR.

3.2. Static powder beds

3.2.1. Powder porosity

Fig. 6 shows porosity values for different powder mixtures. The

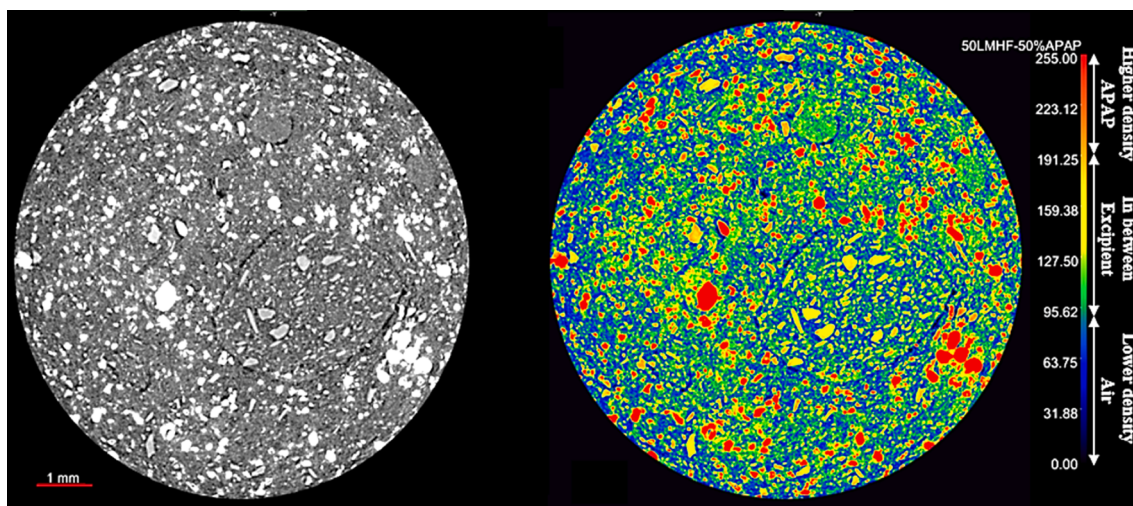


Fig. 4. A cross-sectional axial view of the 50LF-50A powder bed. Left: X-ray microtomography. Right: The color mapping enables the distinction of the three main powder components: Air with lower density (dark blue-light blue), a particle with medium density (green - orange), and a particle with higher density (red).

Table 2
Physical properties of pharmaceutical powders.

Powder Component	Median particle size, d_{50} (μm)	Surface mean diameter, d_s (μm)	Particle skeletal density, ρ_p (g/cm^3)	Particle bulk density, ρ_{bed} (g/cm^3)	Aspect ratio (AR)	Contact angle, θ ($^\circ$) with isopropanol ^a	Contact angle, θ ($^\circ$) with water ^a
Lactose Monohydrate (LMH)	47.9 ± 2.3	21.1	1.543 ± 0.004	0.559	1.83	88.4 ± 0.4	82.7 ± 0.4
Lactose Monohydrate, fine (LMHF)	16.9 ± 0.5	7.8	1.542 ± 0.007	0.370	–	88.4 ± 1.8	85.3 ± 2.7
Microcrystalline Cellulose (MCC)	110.4 ± 6.6	80.8	1.555 ± 0.009	0.326	2.45	82.2 ± 1.8	–
Microcrystalline Cellulose, fine (MCCF)	31.8 ± 0.1	24.6	1.556 ± 0.010	0.343	–	57.9 ± 3.9	–
Acetaminophen (APAP)	50.9 ± 3.9	17.1	1.701 ± 0.001	0.539	2.59	87.5 ± 0.4	–

^a (Li et al., 2021).

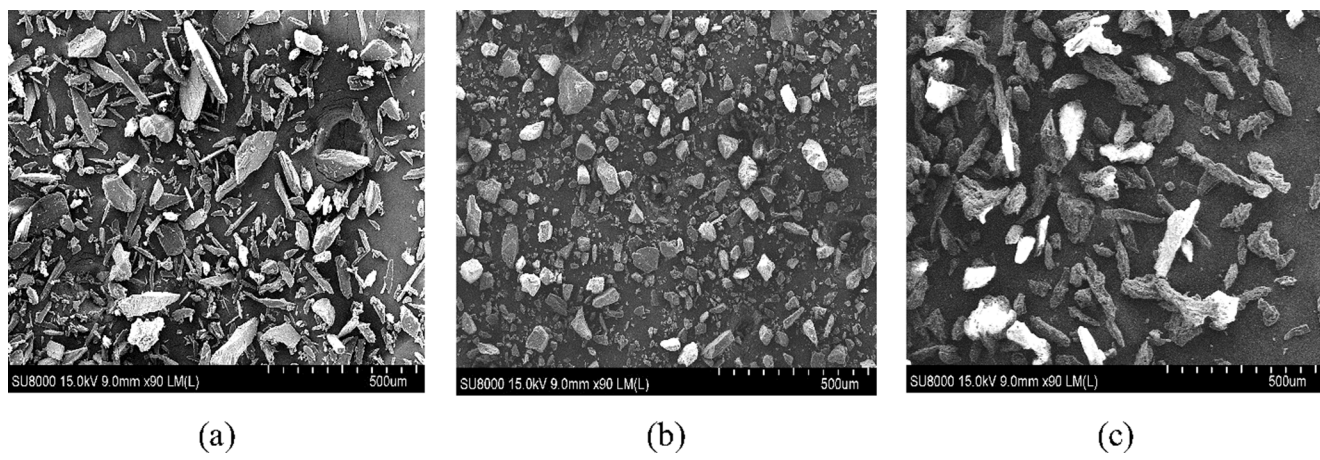


Fig. 5. SEM images of powders: (a) APAP, (b) LMH, and (c) MCC.

porosity of a powder bed is affected by the following factors: particle size, morphology, texture, spatial distribution, bulk density, and processing conditions (Aulton, 2002). Particle size differences in binary mixtures play a vital role in porosity (Dias et al., 2004). Among different powders investigated in this work, LMH and APAP have very close particle sizes and bulk densities (higher compared to others), so the particles properly fill the pores, and thus by increasing the APAP content, the porosity was found to decrease. LMHF-APAP binary mixtures

had higher porosities compared to those for LMH-APAP binary mixtures. In LMHF mixtures, there are some discrete local dense areas, resulting in a porosity increase. Because the inter-particle attractive forces can prevent tiny dry particles (usually $< 100 \mu\text{m}$) from moving freely, agglomerates will be formed, resulting in a porosity increase (Capece et al., 2014). Due to the similar sizes of MCC-APAP and MCCF-APAP, similar porosities were observed. MCCF had a slightly higher bulk density and made powder beds with lower porosities. In general, for particles of

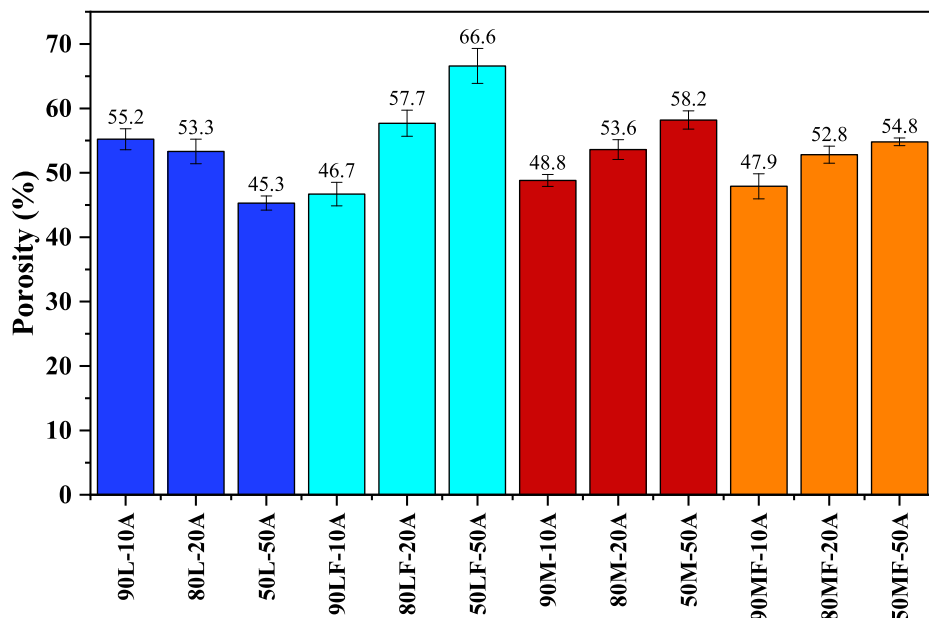


Fig. 6. Measured porosity for different powder compositions. (dark blue) LMH mixtures; (light blue) LMHF mixtures; (red) MCC mixtures; (orange) MCF mixtures.

different sizes, there is an additional void space between different particles (El-Husseiny et al., 2019). As a result, by increasing the portion of the active component (reaching 50 %), the porosity is expected to

increase; this was more obvious in the case of LMHF-APAP, as increasing the APAP fraction resulted in significantly higher porosity.

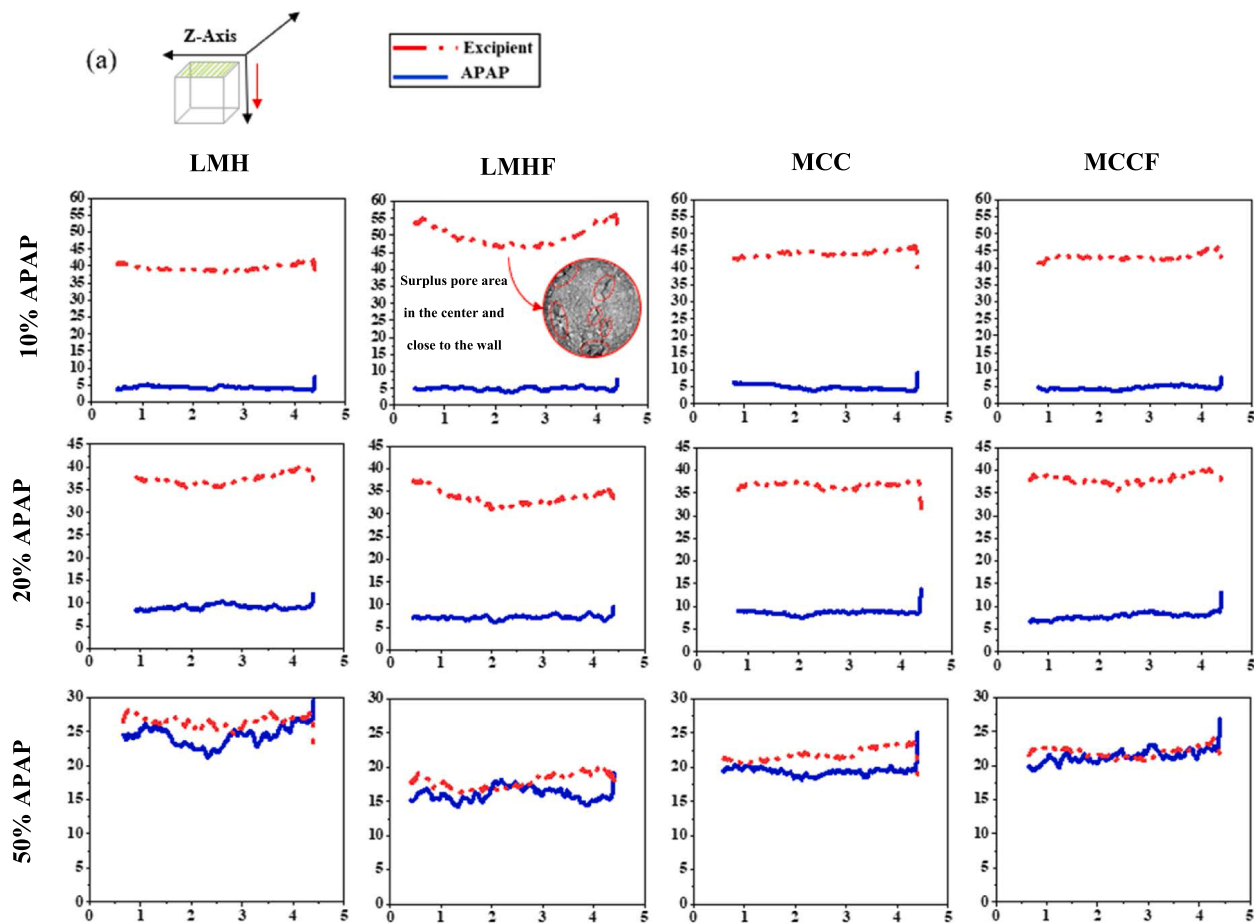


Fig. 7. Area percentage of different particles at different distances from the origin of volume for different compositions. (a) along Z, (b) along Y. Y-axis: Particles content (%), X-axis: Distance from the origin (mm).

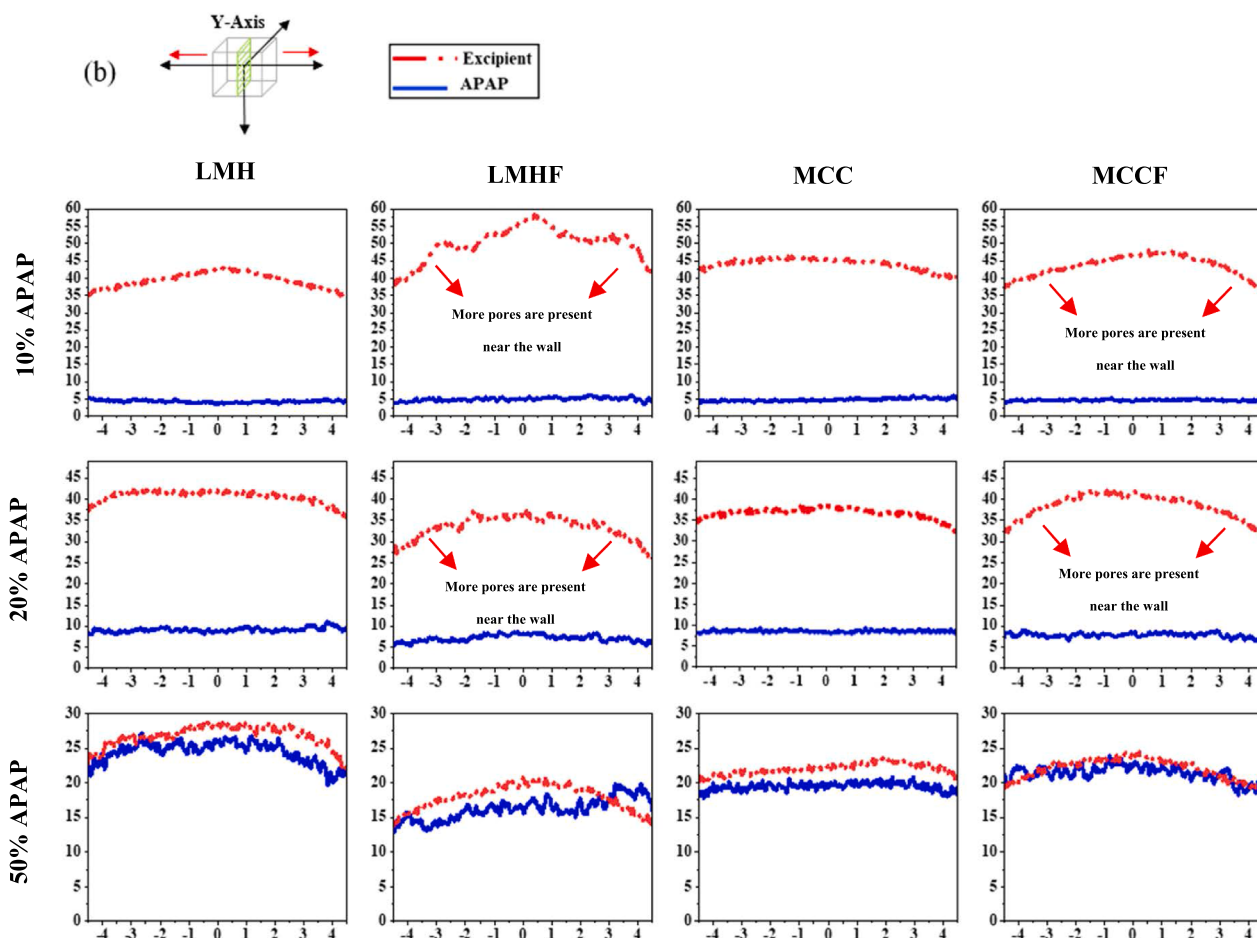


Fig. 7. (continued).

3.2.2. Particles distribution along axes and agglomeration status

Fig. 7 shows the percent of area occupied by API and excipients along the Y and Z directions. Showing how much of the area is covered by a specific particle at any distance from the green origin indicated in Fig. 7, along the height or diameter of the powder bed in FOV. The zero values in the plots (Fig. 7a) indicate the air space at the top of the powder. According to the plots along the Y direction (Fig. 7b), there were more pores available near the wall than in the center, which was more dominant in mixtures of fine powders.

In general, smoother trends with fewer fluctuations represented less agglomeration inside the powder bed, so the agglomeration possibility in a lower percentage of APAP (10 %) was less in both coarse and fine particles. Because of the effects of inter-particle forces, agglomeration increased in all samples as the active component was increased. Overall, in accordance with previous studies (Chaudhuri et al., 2006; Venables and Wells, 2001), agglomeration increased when switching from coarse to fine particles. As a result, macro voids formed within the fine powders, as demonstrated by 90 % LMHF (See Fig. 7a). Also, agglomeration was less in MCC mixtures than in other compositions, mainly due to the better flowability of MCC particles.

In a batch mixing process, blend homogeneity is dependent on blending time and types of excipients (Jaspers et al., 2022). Powder uniformity was quantified by determining the drug content (data derived from Fig. 7a) through 800 slices along the Z direction in the FOV (see Fig. 2). The relative standard deviation (RSD) over average drug concentration was measured to determine the powder uniformity along the Z direction. A lower RSD indicates a better mixing quality in the powder.

The RSD values of the API concentration for different powder

compositions are shown in Fig. 8. Generally, at a lower fraction of APAP, a lower mixing quality was achieved (Oka et al., 2015). 90M–10A had the largest RSD value, as MCC and APAP had different particle sizes and shapes. In contrast, at 50 % of the excipients, MCC and MCCF mixtures contributed to better mixing quality. The reason is due to the tendency for agglomeration in LMH and LMHF mixtures (see Fig. 7a), which is a common type of segregation when handling particles (Tang and Puri, 2004).

3.3. Penetration dynamics

Both 2D radiography and 3D microtomography techniques were applied to visualize liquid binder droplet penetration inside the powder bed. Fig. 9 illustrates the granulation procedure in the spray zone in the wet granulator, and due to the very fast first steps and artifacts problem, 2D images are used for illustration. This study focuses on the droplet penetration stage (Fig. 9c).

A 50 % excipient fraction was set for different powders. Because the penetration of 50M–50A with deionized water occurred in less than 200 ms, there were too many artifacts preventing a good analysis, so 50LF–50A and 50L–50A were chosen to compare the two binders. Based on the experiments, for most powder cases, the granulation took place simultaneously while the droplet was penetrating, so penetration time in this study was defined as the time from the beginning of the penetration (Fig. 9c) to the point that the contact angle remained unchanged and the droplet height was positive based on the defined base. Due to the porous nature of the powder bed and the velocity and weight of the droplet, after the first impact of the droplet, there was a crater formed on the powder surface (see Fig. 10), but after that, the surface was pinned

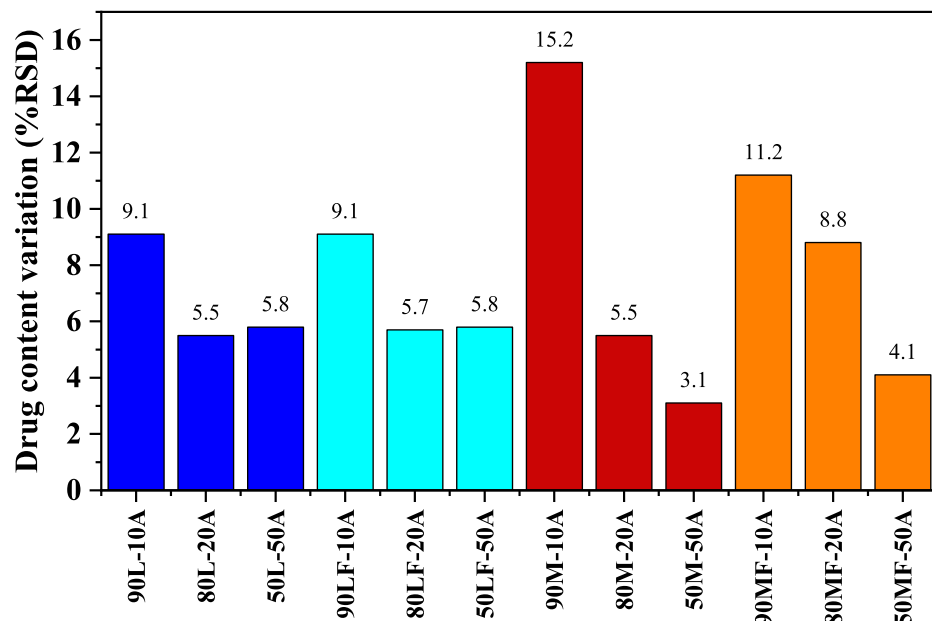


Fig. 8. RSD represents binary mixtures' uniformity. (dark blue) LMH mixtures; (light blue) LMHF mixtures; (red) MCC mixtures; (orange) MFCCF mixtures.

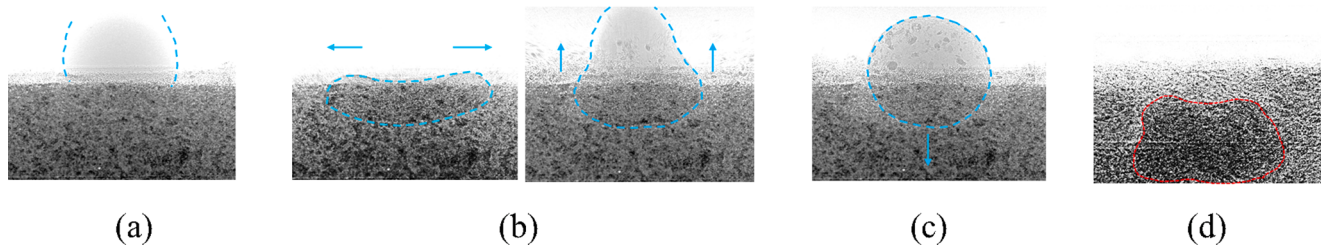


Fig. 9. The four steps of granulation. The droplet is indicated with a blue dashed line, and the final granule is shown by a red dashed line (the wet final granule, as a denser area, is darker compared to the surroundings). (a) droplet impact; (b) droplet spreading and rebound; (c) droplet penetration into the powder pores and wetting; (d) nucleation and granule formation.

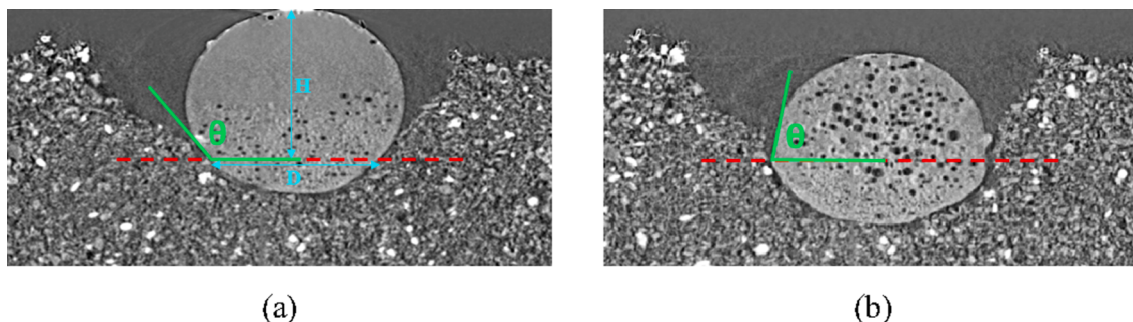


Fig. 10. Illustration of droplet penetration parameters, 50L-50A with deionized water. The red dashed line is the base, where droplet and powder contact ends. (a) during the penetration, (b) endpoint.

during the penetration. To relate the powder bed structural properties and the droplet spreading and imbibition behavior, droplet width (D), maximum droplet height (H), and dynamic contact angle (θ) with time were measured (see Fig. 10). To be consistent in the measurements, the base was set for each composition, considering the image sequences and final granule status (red dashed line in Fig. 10).

Different powders had different ranges for the penetration parameters. The time was normalized by t^* , corresponding to the time the penetration process finished. Droplet and height evolution and contact angle decay were normalized with respective initial values. So, in order to compare the imbibition/spreading behavior of the droplet, some

dimensionless parameters were defined as below:

$$\bar{t} = \frac{t}{t^*} \quad (5)$$

$$\bar{D} = \frac{D}{D_0} \quad (6)$$

$$\bar{H} = \frac{H}{H_0} \quad (7)$$

$$\bar{\theta} = \frac{\theta}{\theta_0} \quad (8)$$

where t^* , D_0 , H_0 and θ_0 are final penetration time, initial droplet width, initial droplet height from the bed surface, and initial contact angle, respectively. The summary of penetration parameters for different powders is provided in Table 3. The parameters include penetration time, t^* , maximum spreading width, which is the maximum droplet width, D_M , and maximum contact angle, θ_M .

LMH and LMHF had a larger static contact angle with isopropanol than those for MCC and MCCF, as well as fewer uniform particles and less uniform pore distribution (see Fig. 7), and these properties prevented the droplet from penetrating (Hapgood et al., 2002). As such, the droplet penetrated much more slowly with a shorter penetration length. Fig. 11 shows a clear visualization of the dynamic droplet penetration. These images are cross-sectional views from a 3D volume.

Porosity had a greater impact on the penetration time than the static contact angle with the liquid binder, according to Shi et al. (2019). Both LMHF and LMH had the same contact angle with isopropanol, but 50LF-50A had a higher porosity than 50L-50A (see Fig. 6), resulting in a shorter penetration time. Agglomeration and non-uniformity of the powder bed were other significant factors affecting the penetration time. As shown in Fig. 7, the 50MF-50A sample with less uniformity and a lower porosity than that of 50M-50A had a longer penetration time. Both 50LF-50A and 50L-50A had a much longer penetration time with water than isopropanol. LMH was soluble in water (Mundoza et al., 2018), and partial dissolution and intermediate viscous forces slowed down the imbibition considerably. The presence of powders on the droplet surface and simultaneous dominant nucleation (see Fig. 11b) prevented the droplet from penetration, so internal porosity did not play an important role. In addition, as LMHF had a higher contact angle with water compared to LMH, the penetration/granulation process of the LMHF powders was longer.

3.3.1. Droplet geometry

To compare the droplet shape evolution with time, changes in its width and height were normalized over time, and are shown in Fig. 12.

The changes in the droplet width were minimal (Fig. 12a), with the greatest change being a 17 % increase in 50L-50A-W. And, because the changes were small, the droplet width was assumed to remain constant during the penetration. Both fine and coarse powders with the same binder showed very similar behavior regarding the droplet width evolution.

As mentioned earlier, the droplet height was smoothly reduced due to the uniform pore distribution of the MCC powders. In contrast, particularly in LMH and LMHF, the droplet height (isopropanol) initially decreased at a faster rate, which could be attributed to the presence of larger pores at the beginning of the droplet path, thereby enhancing flow (Mundoza et al., 2018). The lower \bar{H} ratio at the end indicates that a significant amount of the droplet was absorbed after the first impact, which could be due to the pore structure or a lower static contact angle (higher wettability with the binder), which can be seen in MCC and MCCF mixtures. Both LMH and LMHF with water showed different penetration patterns from all isopropanol compositions. From the first impact of the droplet, powders attach to the droplet surface (see

Fig. 11b). Therefore, because of the simultaneous wetting and nucleation, the droplet height did not change noticeably. As a result, there was no significant imbibition. However, these droplets tended to spread horizontally (see Fig. 12a).

3.3.2. Dynamic droplet volume and contact angle

Fig. 13a shows the volume changes of a droplet before complete imbibition. Volume changes for MCC-MCCF follow the \sqrt{t} trend based on single-phase Darcy's law, which assumes a 1D flow (Yin et al., 2018). However, liquid droplet penetration is a 3D process (Mundoza et al., 2018). It can be concluded that for MCC-MCCF mixtures, as the power values were closer to 0.5, during the penetration, the droplet tended to imbibe rather than spread, which was in agreement with the uniform pore distribution inside the powder (see Fig. 7). In addition, due to the MCC-MCCF structure (see Fig. 4), rod-shaped pores were present as well, enhancing the vertical flow (Shi et al., 2019). For 50LF-50A-W and 50L-50A-W, $V(t)$ remained high due to negligible imbibition and dominant granulation into the droplet from its surface. The power values (low and around 0.2) for power laws deviated greatly with the single-phase Darcy's law, implying a very slow or no imbibition into the powder bed.

The dynamic contact angle decreased for all compositions, as clearly shown in Fig. 13b. As there was no significant penetration for 50LF-50A-W and 50L-50A-W, the contact angle did not change much either. While the droplet is penetrating, its width and contact angle change, and the penetration takes place in three probable mechanisms, constant drawing area (CDA), decreasing drawing area (DDA), and increasing drawing area (IDA) (Denesuk et al., 1993; Mundoza et al., 2018). It can be concluded that the droplet penetration inside all powders is described above in the CDA phase, where the dynamic contact angle decreased while the droplet width remained constant (Mundoza et al., 2018).

3.3.3. Vertical imbibition

In all compositions, the gradual rate of imbibition increased (see Fig. 14). Finer particles had a slower imbibition rate, because of the aggregation of fine particles and the presence of local packings and macropores hindering the penetration process. Tortuosity increases when the porosity decreases (Qiao et al., 2012). When compared to others, 50M-50A had higher porosity, which resulted in higher permeability, increased capillary suction, a faster imbibition rate, and a shorter penetration time. Based on the competing imbibition and spreading behavior of droplets, 50MF-50A had almost constant R_{imb} but the greatest changes in the droplet width.

4. Conclusions

This work employed an advanced synchrotron-based X-ray CT technique to investigate the pore structures and dynamic binder droplet penetration in pharmaceutical powders. In the first phase, for powder binary mixtures of LMH and MCC with APAP, the porosity, mixing quality, particles, and pore distribution along different axes were studied. Both coarse and fine excipients with mass fractions of 90 %, 80 %, and 50 % were examined. The lower size ratios between components resulted in lower porosities, which was the case for mixtures of LMH. And, for the particles with different sizes, the porosity increased by

Table 3
Penetration properties.

Powder	Binder	Sample name	Penetration time, t^* (s)	Penetration length, L (mm)	Maximum spreading width, D_M (mm)	Maximum contact angle, θ_M (°)
50L-50A	Isopropanol	50L-50A-I	5.10	0.69	3.05	124
50LF-50A	Isopropanol	50LF-50A-I	5.00	0.78	3.23	125
50M-50A	Isopropanol	50M-50A-I	0.27	0.81	2.94	97
50MF-50A	Isopropanol	50MF-50A-I	0.85	1.01	3.15	125
50L-50A	Deionized water	50L-50A-W	870	1.07	3.05	125
50LF-50A	Deionized water	50LF-50A-W	1,110	1.24	2.77	127

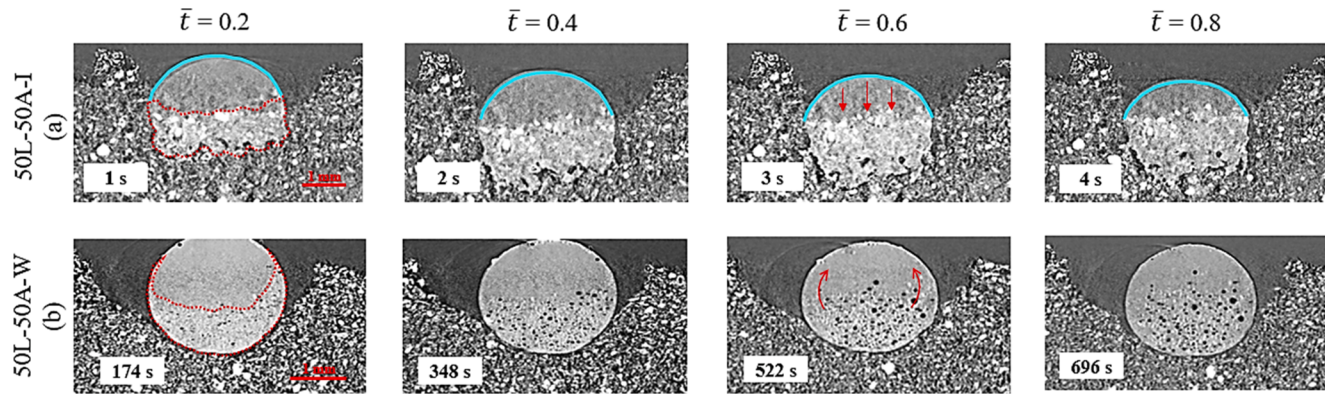


Fig. 11. Time CT images of the droplet penetration at time points $\bar{t} = 0.2, 0.4, 0.6$, and 0.8 . (a) 50L-50A with isopropanol, droplet cap is shown by a blue line and the granule is forming beneath the bed surface. (b) 50L-50A with deionized water, powder covers the droplet and moves inward to form the granule.

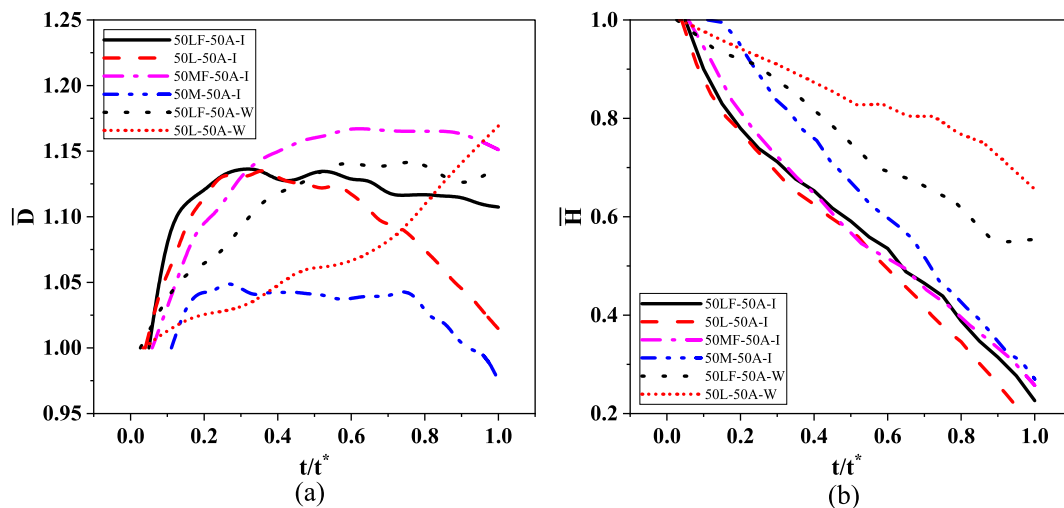


Fig. 12. Droplet width and height dynamics as a function of time. (a) dimensionless droplet width, (b) dimensionless droplet height.

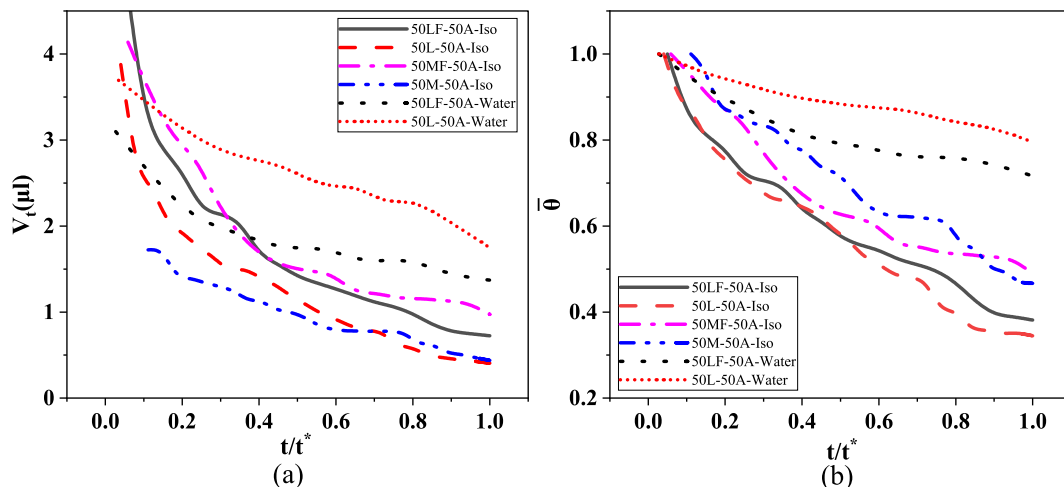


Fig. 13. Droplet volume and contact angle dynamics as a function of time. (a) the volume of droplet remained on the surface and the corresponding power-law fits are as follows: (solid) $y = 0.834x^{-0.689}$, $R^2 = 0.936$; (dash) $y = 0.5606x^{-0.711}$, $R^2 = 0.9015$; (dash dot) $y = 1.0433x^{-0.553}$, $R^2 = 0.9352$; (dash dot dot) $y = 0.5715x^{-0.606}$, $R^2 = 0.9059$; (dot) $y = 1.4675x^{-0.229}$, $R^2 = 0.9655$; (short dot) $y = 2.1609x^{-0.186}$, $R^2 = 0.851$. (b) dimensionless dynamic contact angle.

increasing the amount of one of the components, resulting in the presence of additional void space. MCC powders were found to have less agglomeration and more uniform particle distribution. By increasing the APAP fraction, a better mixing quality was achieved. 50 % of excipients

were set to study the penetration dynamics with the binder of isopropanol and deionized water. Better pore distribution in the path of the droplet penetration was one dominant factor for faster penetration time and shorter penetration length. Also, higher porosity resulted in more

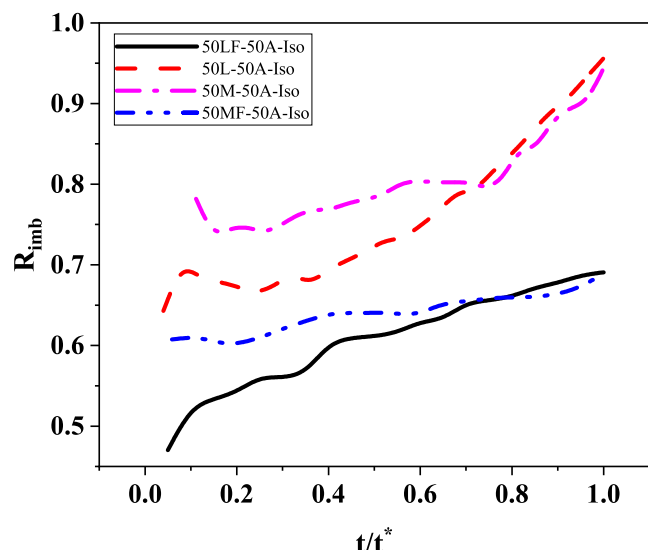


Fig. 14. Imbibition kinetics in dimensionless Darcy's flow.

rapid penetration, as LMHF mixtures had higher porosity than LMH ones, so the droplet penetrated faster. During penetration for all compositions, the dynamic contact angle decreased. There was a competing behavior between spreading and imbibition of a droplet during the penetration process; as for MCCF, the imbibition rate was almost constant, but the droplet width changed more significantly, with a 15 % increase. Both LMH and LMHF showed a different pattern with water; granulation was dominant over penetration because of the particle dissolution inside water.

This study demonstrated that internal observation of the powder bed and visualization of the real-time wetting provide reliable information to select the desired conditions and materials for wet granulation.

CRediT authorship contribution statement

Sima Zeinali Danalou: Conceptualization, Writing – original draft, Methodology, Investigation, Visualization. **Xiao Fan Ding:** Investigation, Writing – review & editing. **Ning Zhu:** Methodology, Writing – review & editing. **Heather N. Emady:** Writing – review & editing. **Lifeng Zhang:** Conceptualization, Writing – review & editing, Supervision, Project administration, Funding acquisition.

Declaration of Competing Interest

The authors declare that they have no known competing financial interests or personal relationships that could have appeared to influence the work reported in this paper.

Data availability

Data will be made available on request.

Acknowledgments

The authors gratefully acknowledge financial support from NSERC and the University of Saskatchewan. Acknowledgments to Jingsi Yang and Carter Blocka from the University of Saskatchewan for their help in doing experiments. We also acknowledge Dr. Sergey Gasilov for the imaging setup development. All of the research described in this paper was performed at the Canadian Light Source, which is supported by the Canada Foundation for Innovation (CFI), the Natural Sciences and Engineering Research Council (NSERC), the National Research Council (NRC), the Canadian Institutes of Health Research (CIHR), the

Government of Saskatchewan, and the University of Saskatchewan.

References

- Asachi, M., Nourafkan, E., Hassanpour, A., 2018. A review of current techniques for the evaluation of powder mixing. *Adv. Powder Technol.* 29, 1525–1549. <https://doi.org/10.1016/j.apt.2018.03.031>.
- Aulton, M.E. (Ed.), 2002. *Pharmaceutics: The Science of Dosage Form Design*, second ed. Elsevier.
- Capece, M., Huang, Z., To, D., Aloia, M., Muchira, C., Davé, R.N., Yu, A.B., 2014. Prediction of porosity from particle scale interactions: Surface modification of fine cohesive powders. *Powder Technol.* 254, 103–113. <https://doi.org/10.1016/j.powtec.2014.01.006>.
- Charles-Williams, H.R., Wengeler, R., Flore, K., Feise, H., Hounslow, M.J., Salman, A.D., 2011. Granule nucleation and growth: Competing drop spreading and infiltration processes. *Powder Technol.* 206, 63–71. <https://doi.org/10.1016/j.powtec.2010.06.013>.
- Chaudhuri, B., Mehrotra, A., Muzzio, F.J., Tomassone, M.S., 2006. Cohesive effects in powder mixing in a tumbling blender. *Powder Technol.* 165, 105–114. <https://doi.org/10.1016/j.powtec.2006.04.001>.
- Clarke, A., Blake, T.D., Carruthers, K., Woodward, A., 2002. Spreading and imbibition of liquid droplets on porous surfaces. *Langmuir* 18, 2980–2984. <https://doi.org/10.1021/la0117810>.
- Denesuk, M., Smith, G.L., Zelinski, B.J.J., Kreidl, N.J., Uhlmann, D.R., 1993. Capillary Penetration of Liquid Droplets into Porous Materials. *J. Colloid Interface Sci.* 158, 114–120. <https://doi.org/10.1006/jcis.1993.1235>.
- Dias, R.P., Teixeira, J.A., Mota, M.G., Yelshin, A.I., 2004. Particulate binary mixtures: Dependence of packing porosity on particle size ratio. *Ind. Eng. Chem. Res.* 43, 7912–7919. <https://doi.org/10.1021/ie040048b>.
- El-Husseini, A., Vanorio, T., Mavko, G., 2019. Predicting porosity of binary mixtures made out of irregular nonspherical particles: Application to natural sediments. *Adv. Powder Technol.* 30, 1558–1566. <https://doi.org/10.1016/j.apt.2019.05.001>.
- Emady, H.N., Kayrak-Talay, D., Schwerin, W.C., Litster, J.D., 2011. Granule formation mechanisms and morphology from single drop impact on powder beds. *Powder Technol.* 212, 69–79. <https://doi.org/10.1016/j.powtec.2011.04.030>.
- Emady, H.N., Kayrak-Talay, D., Litster, J.D., 2013. A Regime Map for Granule Formation by Drop Impact on Powder Beds. *AIChE J.* 59 <https://doi.org/10.1002/aic>.
- Faragó, T., Gasilov, S., Emslie, I., Zuber, M., Helfen, L., Vogelgesang, M., Baumbach, T., 2022. Tofu: a fast, versatile and user-friendly image processing toolkit for computed tomography. *J. Synchrotron Radiat.* 29, 916–927. <https://doi.org/10.1107/s16057752200282X>.
- Forný, L., Marabi, A., Palzer, S., 2011. Wetting, disintegration and dissolution of agglomerated water soluble powders. *Powder Technol.* 206, 72–78. <https://doi.org/10.1016/j.powtec.2010.07.022>.
- Fu, F., Li, P., Wang, K., Wu, R., 2019. Numerical Simulation of Sessile Droplet Spreading and Penetration on Porous Substrates. *Langmuir* 35, 2917–2924. <https://doi.org/10.1021/acs.langmuir.8b03472>.
- Furukawa, R., Shiosaka, Y., Kadota, K., Takagaki, K., Noguchi, T., Shimotsuka, A., Shirakawa, Y., 2016. Size-induced segregation during pharmaceutical particle die filling assessed by response surface methodology using discrete element method. *J. Drug Deliv. Sci. Technol.* 35, 284–293. <https://doi.org/10.1016/j.jddst.2016.08.004>.
- Gao, T., Singaravelu, A.S.S., Oka, S., Ramachandran, R., Štepánek, F., Chawla, N., Emady, H.N., 2018. Granule formation and structure from single drop impact on heterogeneous powder beds. *Int. J. Pharm.* 552 (1–2), 56–66.
- Gao, T., Singaravelu, A.S.S., Oka, S., Ramachandran, R., Štepánek, F., Chawla, N., Emady, H.N., 2020. Powder bed packing and API content homogeneity of granules in single drop granule formation. *Powder Technol.* 366, 12–21. <https://doi.org/10.1016/j.powtec.2020.02.039>.
- Gonçalves, M., Kim, J.Y., Kim, Y., Rubab, N., Jung, N., Asai, T., Hong, S., Weon, B.M., 2022. Droplet evaporation on porous fabric materials. *Sci. Rep.* 12, 1–11. <https://doi.org/10.1038/s41598-022-04877-w>.
- Hapgood, K.P., Litster, J.D., Biggs, S.R., Howes, T., 2002. Drop penetration into porous powder beds. *J. Colloid Interface Sci.* 253, 353–366. <https://doi.org/10.1006/jcis.2002.8527>.
- He, X., Han, X., Ladyzhynsky, N., Deanne, R., 2013. Assessing powder segregation potential by near infrared (NIR) spectroscopy and correlating segregation tendency to tabletting performance. *Powder Technol.* 236, 85–99. <https://doi.org/10.1016/j.powtec.2012.05.021>.
- Iveson, S.M., Litster, J.D., Hapgood, K., Ennis, B.J., 2001. Nucleation, growth and breakage phenomena in agitated wet granulation processes: a review. *Powder Technol.* 117, 3–39. [https://doi.org/10.1016/S0032-5910\(01\)00313-8](https://doi.org/10.1016/S0032-5910(01)00313-8).
- Jaspers, M., Kulkarni, S.S., Tegel, F., Roelofs, T.P., de Wit, M.T.W., Janssen, P.H.M., Meir, B., Weinikötter, R., Dickhoff, B.H.J., 2022. Batch versus continuous blending of binary and ternary pharmaceutical powder mixtures. *Int. J. Pharm.* X 4, 100111.
- Jianzhuang, L., Wenqing, L., Yupeng, T., 1991. Automatic thresholding of gray-level pictures using two-dimension Otsu method. In: China., 1991 International Conference on Circuits and Systems, vol. 1, pp. 325–327. <https://doi.org/10.1109/CICCAS.1991.184351>.
- Kalender, W.A., 2011. *Computed tomography Fundamentals, System Technology, Image Quality, Applications*. Publicis Publishing, Erlangen.
- Lacey, P.M.C., 1954. Developments in the theory of particle mixing. *J. Appl. Chem.* 4, 257–268. <https://doi.org/10.1002/jctb.5010040504>.
- Li, C., Zhu, N., Emady, H.N., Zhang, L., 2019. Synchrotron-based X-ray in-situ imaging techniques for advancing the understanding of pharmaceutical granulation. *Int. J. Pharm.* 572, 118797. <https://doi.org/10.1016/j.ijpharm.2019.118797>.

- Li, C., Zhang, Y., Zhu, N., Emady, H.N., Zhang, L., 2021. Experimental investigation of wet pharmaceutical granulation using in-situ synchrotron X-ray imaging. *Powder Technol.* 378, 65–75. <https://doi.org/10.1016/j.powtec.2020.09.063>.
- Marone, F., Schlepütz, C.M., Martí, S., Fusseis, F., Velásquez-Parra, A., Griffa, M., Jiménez-Martínez, J., Dobson, K.J., Stampaoni, M., 2020. Time Resolved in situ X-Ray Tomographic Microscopy Unraveling Dynamic Processes in Geologic Systems. *Front. Earth Sci.* 7 <https://doi.org/10.3389/feart.2019.00346>.
- Mundoza, A.L., Cartwright, J.J., Tridon, C.C., Hounslow, M.J., Salman, A.D., 2018. Hydrophobic/hydrophilic static powder beds: Competing horizontal spreading and vertical imbibition mechanisms of a single droplet. *Powder Technol.* 330, 275–283. <https://doi.org/10.1016/j.powtec.2018.02.032>.
- Oka, S., Emady, H., Kašpar, O., Tokárová, V., Muzzio, F., Štěpánek, F., Ramachandran, R., 2015. The effects of improper mixing and preferential wetting of active and excipient ingredients on content uniformity in high shear wet granulation. *Powder Technol.* 278, 266–277. <https://doi.org/10.1016/j.powtec.2015.03.018>.
- Oka, S., Sahay, A., Meng, W., Muzzio, F., 2017. Diminished segregation in continuous powder mixing. *Powder Technol.* 309, 79–88. <https://doi.org/10.1016/j.powtec.2016.11.038>.
- Otsu, N., 1979. A Threshold Selection Method from Gray-Level Histograms. *IEEE Trans. Syst. Man. Cybern.* 9, 62–66. <https://doi.org/10.1109/TSMC.1979.4310076>.
- Pan, B., Clarkson, C.R., Atwa, M., Debuhr, C., Ghanizadeh, A., Birss, V.I., 2021. Wetting dynamics of nanoliter water droplets in nanoporous media. *J. Colloid Interface Sci.* 589, 411–423. <https://doi.org/10.1016/j.jcis.2020.12.108>.
- Qiao, Z., Wang, Z., Zhang, C., Yuan, S., Zhu, Y., Wang, J., 2012. PVAm–PIP/PS composite membrane with high performance for CO₂/N₂ separation. *AIChE J.* 59, 215–228. <https://doi.org/10.1002/aic>.
- Shi, Y., Tang, G.H., Lin, H.F., Zhao, P.X., Cheng, L.H., 2019. Dynamics of droplet and liquid layer penetration in three-dimensional porous media: A lattice Boltzmann study. *Phys. Fluids* 31 (4), 042106.
- Tang, P., Puri, V.M., 2004. Methods for minimizing segregation: A review. *Part. Sci. Technol.* 22, 321–337. <https://doi.org/10.1080/02726350490501420>.
- Venables, H.J., Wells, J.I., 2001. Powder mixing. *Drug Dev. Ind. Pharm.* 27, 599–612. <https://doi.org/10.1081/DDC-100107316>.
- Vogelgesang, M., Farago, T., Morgeneyer, T.F., Helfen, L., Dos Santos Rolo, T., Myagotin, A., Baumbach, T., 2016. Real-time image-content-based beamline control for smart 4D X-ray imaging. *J. Synchrotron Radiat.* 23, 1254–1263. <https://doi.org/10.1107/S1600577516010195>.
- Yin, X., Aslannejad, H., de Vries, E.T., Raoof, A., Hassanzadeh, S.M., 2018. Droplet Imbibition into Paper Coating Layer: Pore-Network Modeling Simulation. *Transp. Porous Media* 125, 239–258. <https://doi.org/10.1007/s11242-018-1116-0>.